A spectral induced polarization instrument using square-wave current injection to track critical zone processes: application to long-term monitoring of a wetland

Florence Nicollin, Bruno Kergosien, Léa Lévy, Laurent Longuevergne, Damien Jougnot

Geophysical Journal International

Geophys. J. Int. (2026) **245,** 1–14
Advance Access publication 2026 February 11
Research Paper

https://doi.org/10.1093/gji/ggag060

A spectral induced polarization instrument using square-wave current injection to track critical zone processes: application to long-term monitoring of a wetland

Florence Nicollin,[1] Bruno Kergosien,[1] Léa Lévy,[1] Laurent Longuevergne[1] and Damien Jougnot[2]

[1]*Université de Rennes, CNRS, Géosciences Rennes, UMR* 6118, F-35000 *Rennes, France. E-mail: florence.nicollin@univ-rennes.fr*
[2]*Sorbonne Université, CNRS, EPHE, UMR* 7619 *METIS,* F-75005 *Paris, France*

Accepted 2026 January 30. Received 2026 January 30; in original form 2025 June 20

SUMMARY

In the last two decades, the improvement of both instruments and theory, as well as the broadened scope of applications, led to a spectacular development of the use of induced polarization. In particular, the richness of complex conductivity spectra is driving the scientific community towards vast deployment of this measurement method often referred to as spectral induced polarization (SIP). In this contribution, we describe an innovative multichannel instrument that we develop for fast monitoring of critical zone processes. The spectral content of a signal with line spectrum resulting from square-wave current is exploited by injecting successively three square-wave currents with periods of 1, 10 and 100 s, covering the frequency range of 10^{-2} to 10^{2} Hz in less than 4 min. One data set consists of eight successive current injections at different depths. For each current injection, the electrical potential is simultaneously measured at seven dipoles. The time-series are recorded with a 2 kHz sampling rate, allowing to calculate by Fourier transform the amplitude and phase spectra up to 1 kHz for each quadrupole. The complex conductivity data was validated by a comparison with the commercial SIP-Fuchs instrument, despite a significant discrepancy below 0.1 Hz which may be due to a worse signal-to-noise ratio at low frequencies. The prototype version of the instrument has been installed in 2018 at a wetland at Ploemeur-Guidel hydrogeological observatory to monitor reactive processes with high spatial resolution across the top metre of soil. The instrumental device, controlled by a Gantner data acquisition system connected to a solar panel, is fully autonomous and consumes little energy. Acquisitions are made several times a day and recorded on a SD card. Seven-year continuous monitoring highlights significant temporal variations of both subsurface resistivity and phase angle. The absence of correlation between resistivity and phase variations in the continuously saturated soil thickness highlights the potential of the system to monitor and separate different types of dynamics processes, such as groundwater/surface water mixing and mineral precipitation/dissolution.

Key words: Electrical properties; Induced polarization; Hydrogeophysics.

1. INTRODUCTION

Understanding subsurface reactive transport processes and their response time remains a major challenge for studying the critical zone, for understanding the dynamics of natural biogeochemical cycles, as well as that of contaminations (J. Gaillardet 2023). However, as pointed out in J. Gaillardet *et al.* (2018), critical zone dynamics and reactivity can range over several orders of magnitude in terms of time, making its observation a difficult task. This highlights the need for new instruments that can provide continuous observations of biotic and abiotic interactions at relevant spatial and temporal scales (e.g. event response, seasonal variation, longer time of climate change).

Recent developments show the ability of time-lapse geophysical methods to monitor transient subsurface processes in the field (e.g. T. Hermans *et al.* 2023; M. Dumont & K. Singha 2024), such as groundwater-surface water interaction (L.D. Slater *et al.* 2010), water absorption by roots (D.H. Jayawickreme *et al.* 2010; B. Mary *et al.* 2020) and 3-D migration of gas plumes (C.M. Steelman *et al.* 2017). Furthermore, the potential of induced

polarization methods for monitoring reactive processes has been illustrated by laboratory (e.g. D. Ntarlagiannis *et al*. 2005; L. Slater *et al*. 2007; A. Mellage *et al*. 2018; S. Izumoto *et al*. 2022; F. Rembert *et al*. 2024), and field studies (K.H. Williams *et al*. 2009; A. Flores-Orozco *et al*. 2011; L. Lévy *et al*. 2024), although many questions on the origin of the measured IP signal still remain.

Induced polarization (IP) measurements consist in applying an electric current, and measuring the transient voltage, caused by electric charges accumulation at interfaces between conducting and insulating media, in response to the current (C. Schlumberger 1920; J. Bertin & J. Loeb 1976; J.S. Sumner 1976). The injected current can either have a square or a sinusoidal waveform. When square-wave currents are injected, the method is often called 'time-domain' IP, while it is called 'frequency-domain' IP when a sinusoidal current is injected (e.g. A. Binley & L. Slater 2020).

Petrophysical calibrations between IP signals and physicochemical parameters of interest are necessary to quantitatively interpret field signals. Most of these calibrations are established by laboratory experiments using sinusoidal signals and sweeping over a large frequency range, typically from mHz to kHz. With this approach, the broad-band impedance spectrum (often expressed as amplitude and phase) of the studied medium can be obtained. A few laboratory studies derive petrophysical relations from square-wave IP signals, using either the integral chargeability (K. Titov *et al*. 2004) or spectral information obtained from a relaxation time distribution (K. Titov *et al*. 2002; M. Tong & H. Tao 2007). Overall, most relevant petrophysical relations for interpreting physicochemical processes in the field need impedance spectrum to be applied. While most laboratory-based petrophysical calibrations obtain impedance spectrum based on sinusoidal IP signal, this approach remains time-consuming to be widely deployed in the field (T. Dahlin & V. Leroux 2012; G. Fiandaca *et al*. 2013)—even though it has been successfully applied in a few cases (A. Flores-Orozco *et al*. 2011).

A few approaches exist to extract spectral information from square-wave IP data (G. Fiandaca *et al* 2013; W. Liu *et al*. 2017; W. Liu *et al*. 2019; S. Johansson *et al*. 2020). The approach developed by G. Fiandaca *et al*. (2013) proposes Cole-Cole models in the frequency space, transforms the resulting impedance spectrum into IP time-series for a given current waveform, including square-wave signals typical of field studies, and tries to find the Cole-Cole model that best matches the decaying voltage data by going back-and-forth between the frequency and time domains. This approach allows inverting for the four Cole-Cole parameters but has several drawbacks: (i) the data is parametrized assuming a Cole-Cole model, which is often problematic, (ii) the Cole-Cole model is poorly constrained at low frequency—that is, close or below to the period of the square wave, (iii) the model optimization is carried out using a black box algorithm in the frequency space while the impedance spectrum corresponding to the data itself is never calculated and (iv) there is no open-source code allowing that procedure. Another approach consists in Debye decomposition (S. Nordsiek & A. Weller 2008), which presents the advantage of providing comparable parameters in time and frequency domains (G. Gurin *et al*. 2013; T. Martin *et al*. 2021) but only when some conditions are met, such as a sufficient length of the current step. In addition, Debye decomposition has limitations: (i) the decomposition acts as a noise amplifier (L. Lévy *et al* 2024), (ii) a relaxation time distribution as well as average parameters can be extracted but not the impedance spectrum itself and (iii) the Debye decomposition may differ depending on which portion of the signal is analysed.

Therefore, for many applications, there is need for a methodology that allows rapid data acquisition in the field, that is, relying on square-wave signals as in most field studies, while at the same time allowing the transformation of the time-series into reliable impedance spectra. Such methodology is required to apply in a consistent way laboratory-established petrophysical relations based on spectral IP (SIP). In the specific context of critical zone monitoring, the SIP acquisition methodology must fulfill additional criteria of relatively low production cost and energy consumption, in order to operate in an autonomous way over long periods of time for site-based monitoring.

The main aim of this paper is to present the development of a relevant SIP instrument, the corresponding data acquisition design and processing algorithm. The secondary aim of this paper is to show the quality of SIP monitoring data and their potential to address important environment questions, in this case by monitoring critical zone processes at a natural wetland for nearly seven years. The methodology developed here follows the steps of other long-term, regular, geophysical monitoring methods, such as resistivity monitoring of embankment dam integrity (R. Norooz *et al*. 2024) or of soil properties (e.g. G. Blanchy *et al*. 2025), self-potential monitoring for (eco)hydrology (e.g. E.B. Voytek *et al*. 2019; K. Hu *et al*. 2020) and supraconductor gravimetry monitoring to monitor evapotranspiration (e.g. S.D. Carrière *et al*. 2021).

2. MATERIALS AND METHODS

2.1. Description of the SQWA-SIP system

The SQuare-WAve Spectral Induced Polarization system (SQWA-SIP system) measures induced polarization in the frequency domain by exploiting the spectral richness of a square-wave signals. By recording both the electric current injected in this form and the electrical potential of the same form detected synchronously, the complex impedance is obtained by calculating the ratio of the Fourier transform of the two signals.

A T-periodic square-wave signal, defined by:

$$y(t) = 1 \text{ for } T \in [0, T/2[\text{ and } y(t) = -1 \text{ for } T \in [T/2, T[\quad (1)$$

can be decomposed into a Fourier series as follows:

$$y(t) = \frac{4}{\pi}\left[\sin(\omega t) + \frac{1}{3}\sin(3\omega t) + \frac{1}{5}\sin(5\omega t) + \cdots\right] \text{ with } \omega = \frac{2\pi}{T} \quad (2)$$

that is, the odd harmonics with coefficients decreasing in $1/n$. Its frequency spectrum therefore consists of lines at the odd harmonics of the fundamental, with decreasing amplitude in $1/n$. Fig. 1 shows, in red, an example of a square-wave signal in the time and frequency domains.

The amplitude of the synchronous potential depends on the amplitude of the injected current and the geometry and size of the electrode quadrupole. In the frequency domain, the signal-to-noise ratio controls the number of usable harmonics in the current and potential spectra and therefore the bandwidth over which the complex impedance can be calculated. With the measurement settings described in Section 2.2, the signal-to-noise

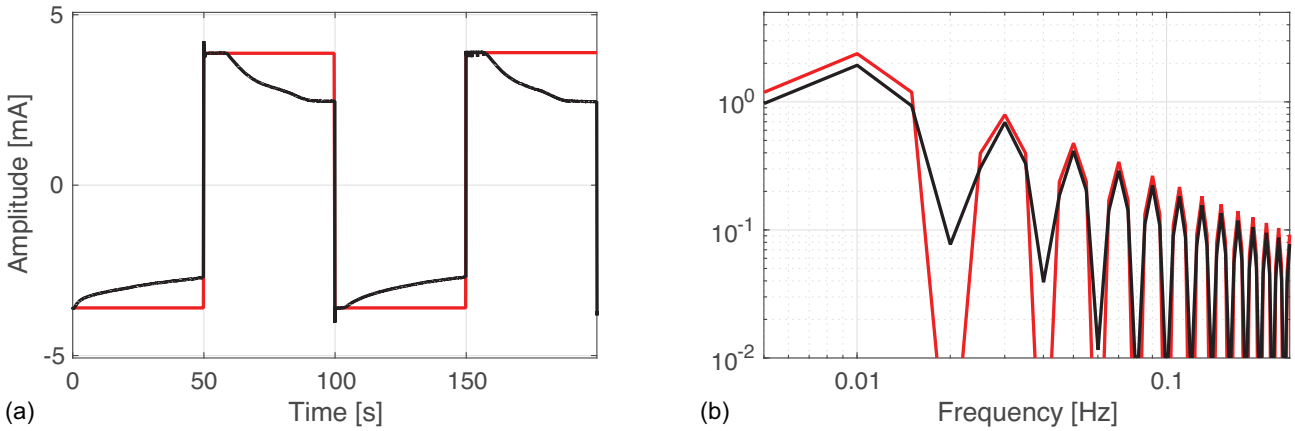

Figure 1. Square-wave signal with a period of 100 s (red line) and example of actual injected current (black line): (a) time-domain data, (b) spectral amplitude. The amplitudes of the ideal square-wave signal are equal to those of the actual signal in the first seconds of each half-period.

ratio allows spectral information to be evaluated over approximately two decades from the fundamental frequency. Thus, using three square-wave signals with periods of 1, 10 and 100 s provides overlapping information over the frequency band from 0.01 to 100 Hz. By successively injecting such currents for two periods each, the total acquisition time is $2 + 20 + 200 = 222$ s, that is, below 4 min. Figs 2(a)–(c) show an example of time-domain data recorded with our SQWA-SIP system. One can see that the current actually injected (black line) is not a perfect square-wave signal, probably due to electrochemical processes or capacitive effects in the coupling of the injection electrodes with the medium. In Fig. 1, the 100 s-period current actually injected is compared to a perfect square-wave signal of the same amplitude in the first seconds of each half-period. Although the injected current is distorted, its spectrum remains a line spectrum at the same frequencies as that of the square-wave signal, with the same amplitude decay. The lines are just slightly broader and slightly weaker in amplitude.

Sampling both current and potential at a frequency rate of 2 kHz allows their frequency spectra, calculated by Fourier transform, to be exploited up to 1 kHz. In the recorded current signals, exactly two periods are selected for each square-wave signal, represented by 4 000 samples for the 1 s-period signal, 40 000 samples for the 10 s-period signal, and 400 000 samples for the 100 s-period signal. In the recorded potential signals, the same periods are selected at exactly the same times (synchronous detection). The Fourier transform of each signal is calculated using Matlab's *fft* function, after removing the DC component and apodizing with a Hanning window. No zero-padding is necessary since the time signal consists of an integer number of periods of the square-wave signal. Thus, the frequency resolution, equal to the ratio between the sampling frequency and the total number of samples, is sufficient to perfectly extract the spectral values at odd harmonics of the fundamental: resolution of 0.5 Hz for the 1 s-period signal (fundamental at 1 Hz), 0.05 Hz for the 10 s-period signal (fundamental at 0.1 Hz), and 0.005 Hz for the 100 s-period signal (fundamental at 0.01 Hz).

The amplitude spectra are plotted with a linear frequency scale in Figs 2(d)–(i), showing the lines at the odd harmonics of the fundamental. In Figs 3(a)–(c), the amplitude spectra are plotted with a logarithmic frequency scale, showing that despite the amplitude decay in $1/n$, the data can be exploited with a good signal-to-noise ratio over two decades from the fundamental frequency.

To estimate the signal-to-noise ratio of the data, we use the self-potential recorded for 1 min before the start of the current injection. Fig. 4(a) shows the spectral amplitude of the self-potential recorded before the SQWA-SIP data of Figs 2 and 3, plotted on the same frequency band. The average noise level calculated up to 1 kHz is equal to 0.17 μV, which is six orders of magnitude lower than the SQWA-SIP potential measured at values of a few hundred mV. A noise at 50 Hz is recorded with an amplitude of 73 μV, which remains much lower than the SQWA-SIP potentials, thanks to the battery power supply of the device (Section 2.2) and the absence of a high-voltage line near the site where the device is installed (Section 2.3). To estimate the signal-to-noise ratio by taking into account the major trends in spectral noise variations, rather than using only its average value, the self-potential spectrum is smoothed by moving average calculated over a decade of logarithmically spaced frequencies. The smoothed curve shows that the noise is higher at low frequencies, with a $1/f$ energy decay up to approximately 10 Hz, where the average level is reached. The signal-to-noise ratio is then calculated using the smoothed self-potential curve interpolated at the odd harmonics over two decades from the fundamental frequency of the three square-wave potential signals (Fig. 4b). The shape of the three curves is mainly controlled by the $1/n$ decay of the line spectrum of the square-wave signals, but despite this decay, the signal-to-noise ratio is always greater than 70 dB and can reach values close to 120 dB. And because of the $1/f$ decay of noise energy at low frequencies, the signal-to-noise ratio at the fundamental frequency of the square-wave signal is better the higher the fundamental frequency.

The complex electrical impedance is obtained at odd harmonic frequencies, by dividing the value of the potential spectrum by that of the injected current spectrum. In order to describe the electrical impedance with a limited number of values according to a progression as logarithmic as possible, only a few values are kept among those calculated at all odd harmonics over two decades from the fundamental frequency (harmonics 1, 3, 5, 7, 9, 11, 13, 17, 21, 25, 33, 49, 65, 97 for the 1 s-period signal; harmonics 1, 3, 5, 7, 13, 17, 23, 37 for the 10 s- and 100 s-period signals). Figs 3(d)–(f) and (g)–(i) show the electrical impedance, in amplitude and phase respectively, at all odd harmonics and at the selected frequencies for the three square-wave signals. The electrical impedance at 30 frequencies between 0.01 and 100 Hz is finally obtained by gathering the selected values for the three signals (Fig. 5).

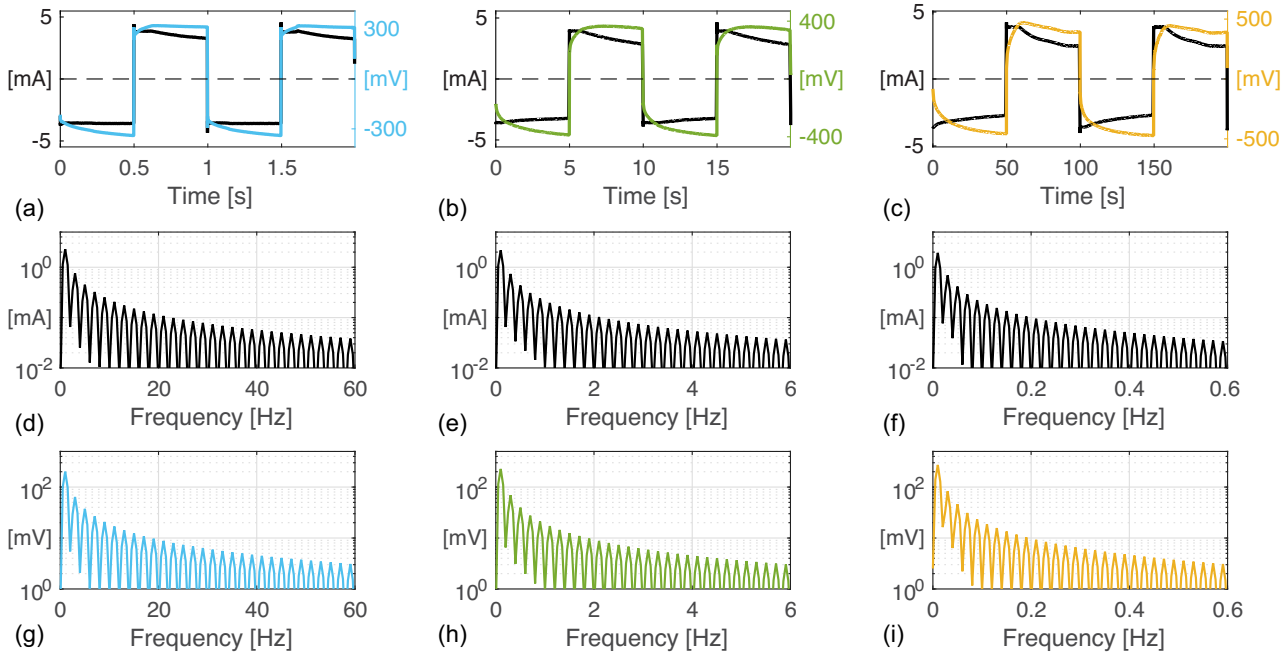

Figure 2. SQWA-SIP time-domain and frequency-domain data: (a, b, c) time-domain data of three square-wave signals (1 s-period signal, 10 s-period signal and 100 s-period signal respectively), in black the injected current, in colour the measured voltage; (d, e, f) Fourier transform amplitude of the injected current plotted with a linear frequency scale; (g, h, i) Fourier transform amplitude of the measured voltage.

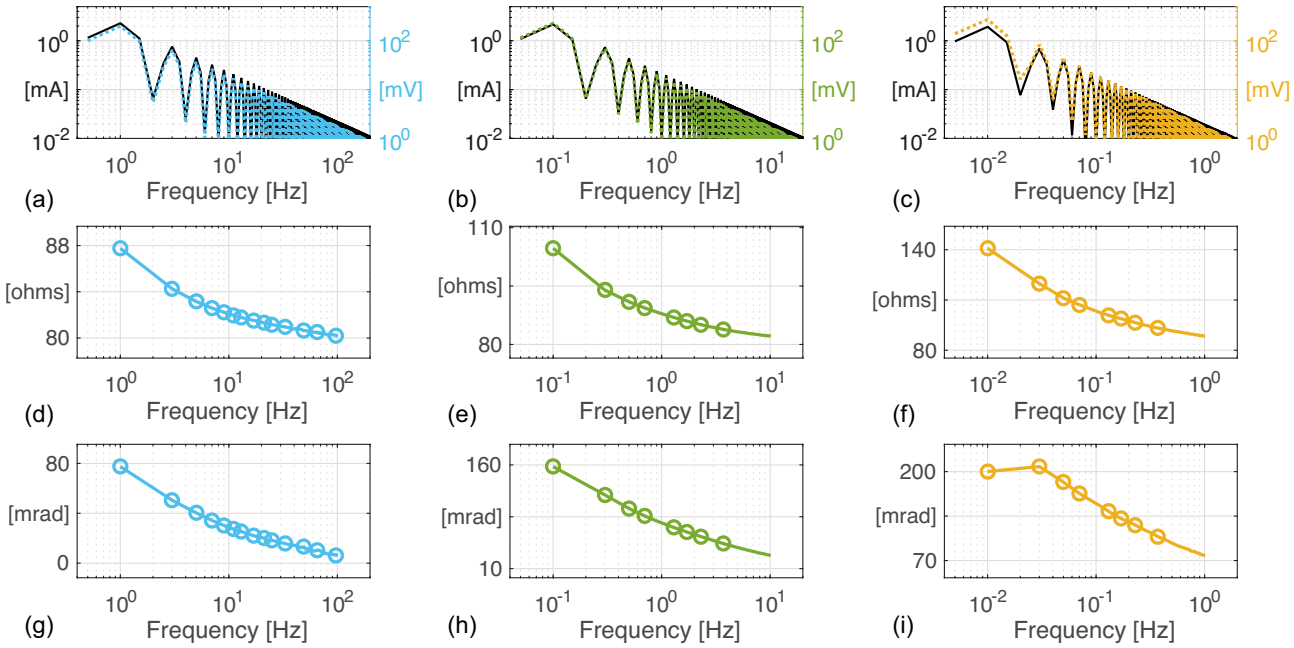

Figure 3. SQWA-SIP frequency-domain data and impedance: (a, b, c) spectral amplitude of the three signals (1 s-, 10 s- and 100 s-period square-wave signals) plotted with a logarithmic frequency scale (solid black line for the injected current, dotted colour line for the measured voltage); (d, e, f) amplitude of the electrical impedance (ratio of the spectral amplitude of potential and current) calculated at the odd harmonics over two decades from the fundamental frequency (solid line), then selected at a few frequencies according to a progression as logarithmic as possible (dots), with 14 values from 1 to 97 Hz for the 1 s-period signal, 8 values from 0.1 to 3.7 Hz for the 10 s-period signal and 8 values from 0.01 to 0.37 Hz for the 100 s-period signal; (g, h, i) phase of the electrical impedance (opposite sign of the phase shift between potential and current) plotted in the same way as the amplitude.

2.2. Electrode design for monitoring critical zone processes

In order to monitor critical zone processes, the SQWA-SIP system is connected to two one-metre-long electrode rods, inserted vertically into the ground a few tens of centimetres apart from each other (Fig. 6). Using a Gantner data acquisition system (Gantner Q.station 101–www.gantner-instruments.com) powered by a 12 V battery connected to a 50 W solar panel, the instrumental device is completely autonomous with the data recorded

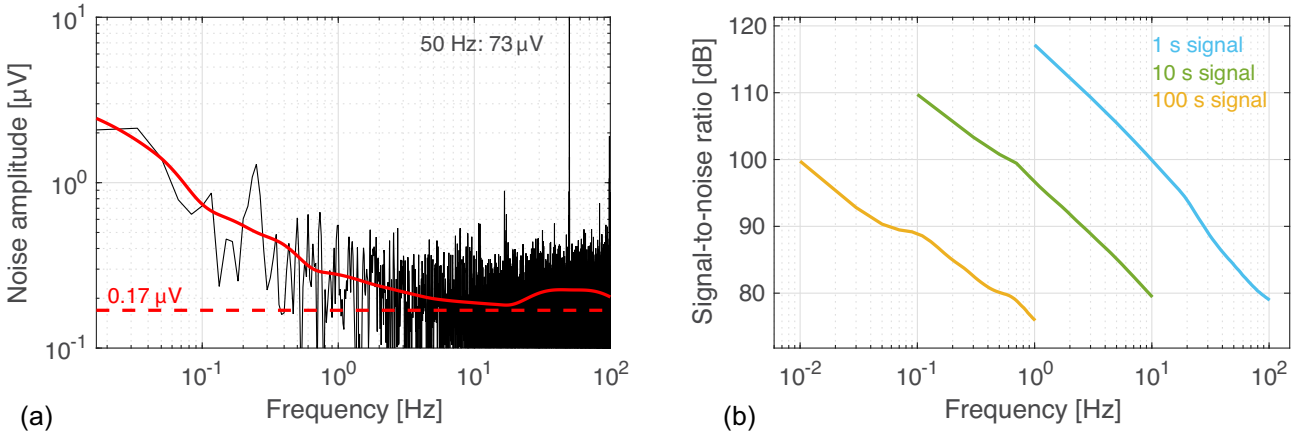

Figure 4. (a) Spectral amplitude of a one-minute recording of the self-potential (black line) and moving average calculated over a decade of logarithmically spaced frequencies (red line); the average value of the self-potential spectrum up to 1 kHz is represented by a red dashed line. (b) Signal-to-noise ratio calculated using the smoothed self-potential curve interpolated at the odd harmonics over two decades from the fundamental frequency of the three square-wave potential signals.

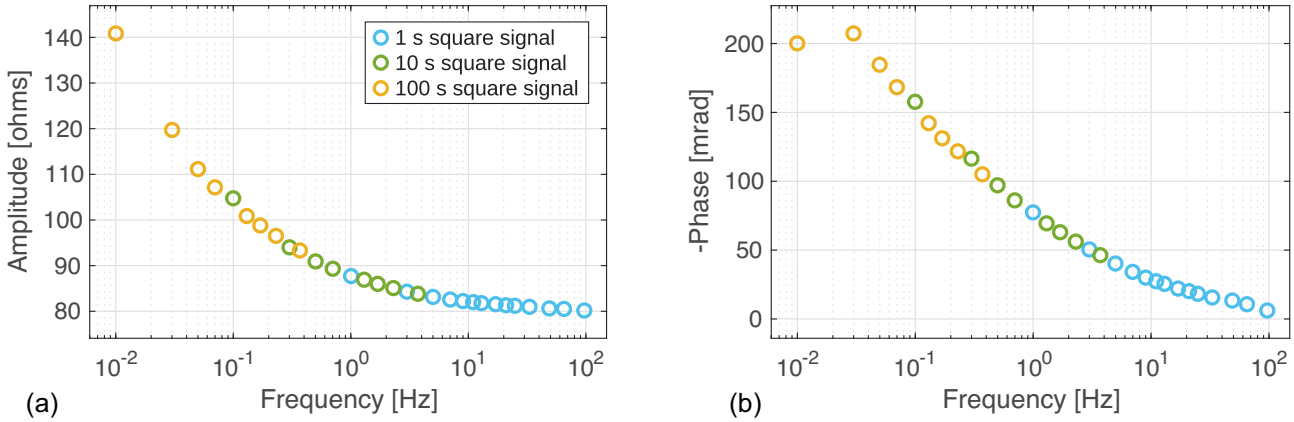

Figure 5. SQWA-SIP electrical impedance obtained from the three signals, at 30 frequency values from 0.01 to 97 Hz: (a) amplitude (ratio of the spectral amplitude of potential and current), (b) phase (opposite sign of the phase shift between potential and current).

on a SD card. It offers 1-D vertical imaging in the top metre of ground with a spatial resolution of the order 5 cm. The rods are made of electrically insulating material, and 15 electrode dipoles are formed between the rods with 5 mm wide stainless steel rings every 5 cm on each rod (Figs 6a and b). The odd-numbered dipoles (E1 to E15) are used successively to inject a current of ±4 mA at eight depths spaced 10 cm apart, while the electric potential is measured simultaneously at the even-numbered dipoles (E2 to E14). The measured data thus provide the electrical impedance of the medium between the current and potential dipoles. If we consider, for example, the measured data with all adjacent current and potential dipoles (E1-E2, E3-E2, E3-E4, ..., E13-E14, E15-E14), the electrical impedance is obtained at 14 depths every 5 cm (Fig. 6a). A relay demultiplexer successively connects each current dipole to the square-wave signal generator, and the voltage of the actual injected current is measured across a 1 Ω shunt (Fig. 6c). The injected current voltage, amplified by 40 dB (Analog Devices 5B-40 signal conditioner), and the seven potential dipoles are measured by an eight-channel differential voltage module (Gantner Q.bloxx A108). The signals are then filtered with a 4th-order low-pass filter at 1 kHz and recorded at a sampling rate of 2 kHz on an SD card. This research-developed instrument is open-source; it is reproducible, flexible and adaptable for other uses.

2.3. Field installation at Ploemeur-Guidel observatory

The Guidel site (L. Guillaumot *et al.* 2022) is a 2.5 km^2 coastal watershed in fractured crystalline rock. Water flow is dominated by aquifer contributions, including deep and long-distance flow lines beyond the topographic catchment. Aquifer discharges into streams and feeds a coastal ecosystem classified as a Natura 2000 site. The mixing of different types of waters (oxygen-rich surface water, iron-rich anoxic deep water, ...) stimulates biogeochemical reactivity (I. Osorio *et al.* 2023) and creates specific habitats. The SQWA-SIP system was set in a lowland and is part of an observation system dedicated to understanding how deep groundwater, flowing up towards the surface, is partitioned as evapotranspiration or river flow. At this place, the depth to groundwater varies from 0 to 25 cm, as shown in Fig. 7, which presents the rainfall readings and the piezometric level recorded over an 18-month period.

The instrumental device was installed at the Guidel wetland in July 2018 (Fig. 6d). The two rods were inserted into the ground 50 cm apart from each other, with the electrodes at depths ranging from 23 to 93 cm, always in a fully saturated medium (Fig. 7b). Until May 2021, injection was limited to a 1 s-period square-wave signal, with successive injection on the eight current dipoles and simultaneous measurement of the potential on

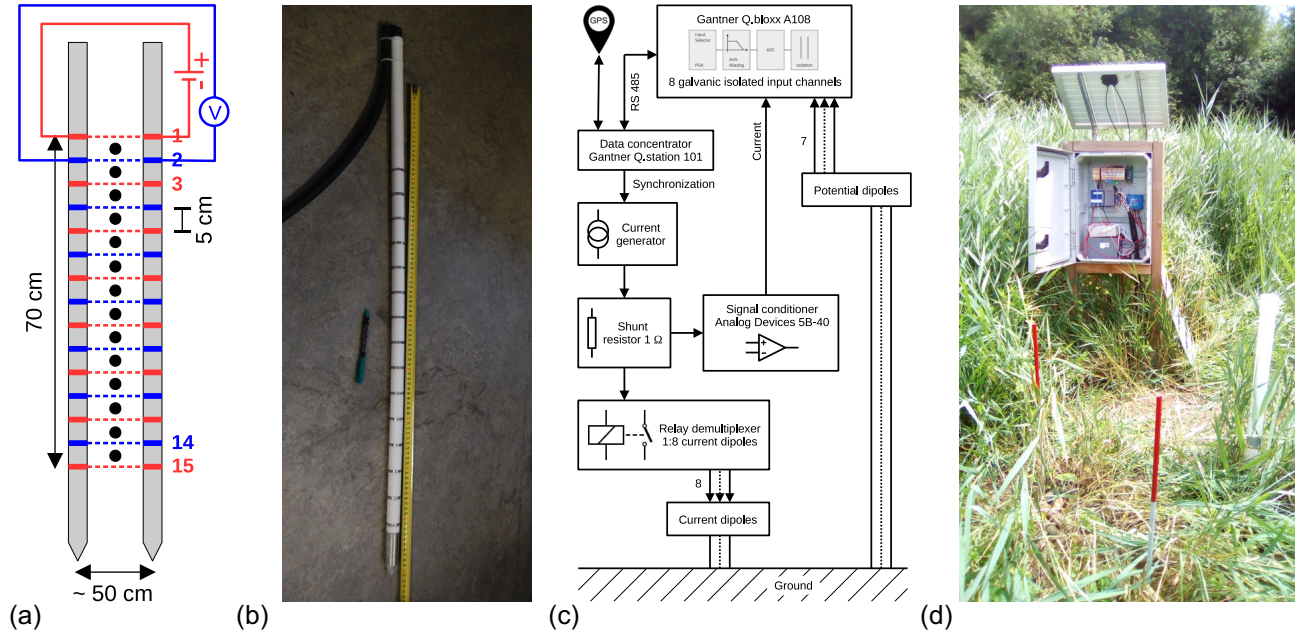

Figure 6. Instrumental device designed for decimetre-scale measurements in the ground: (a) schematic of the rods supporting electrode dipoles numbered from 1 to 15. The eight odd-numbered dipoles (in red) are used to inject current and the seven even-numbered dipoles (in blue) to measure potential. The 14 black dots indicate the location of the measurements obtained with adjacent current and potential dipoles; (b) picture of a rod made of electrically insulating material (white segments), supporting 15 electrodes made of stainless-steel rings every 5 cm; (c) synoptic diagram of the measurement; (d) picture of the instrumental device installed on the field, red sticks indicating the location of the rods.

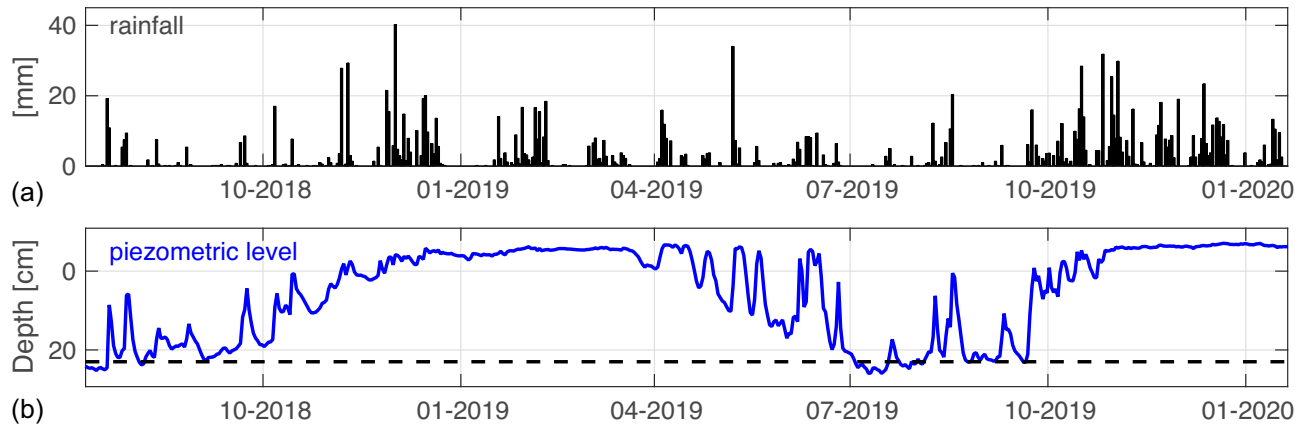

Figure 7. Environmental data in the Guidel wetland: (a) rainfall recorded by a Météo France weather station located 3.5 km away; (b) piezometric level recorded between July 2018 and January 2020 in a small borehole located less than one metre from the electrode rods. The depth of the first electrode dipole is represented by a black dotted line.

the other seven dipoles. The total acquisition time was then less than one minute, and measurements were repeated every four hours. But with the single 1 s-period square-wave signal, the determination of the electrical impedance was limited to the frequency range [1–100] Hz. Since May 2021, the frequency range is extended to lower frequencies, by injecting three square-wave signals with periods of 1, 10 and 100 s. The total acquisition time then amounts to approximately 30 min, and measurements are achieved only twice a day to limit energy consumption to what the battery and solar panel can provide.

3. RESULTS

3.1 Validation measurements on an electrical circuit

First, the SQWA-SIP system was validated by a measurement on a controlled electrical circuit consisting of a 100 Ω resistor in parallel with a 10 μF capacitor. Figs 8(a)–(c) shows that, in the absence of electrodes in contact with the ground, the injected current is a perfect square-wave signal. This tends to confirm that the distortion observed when current is injected in the

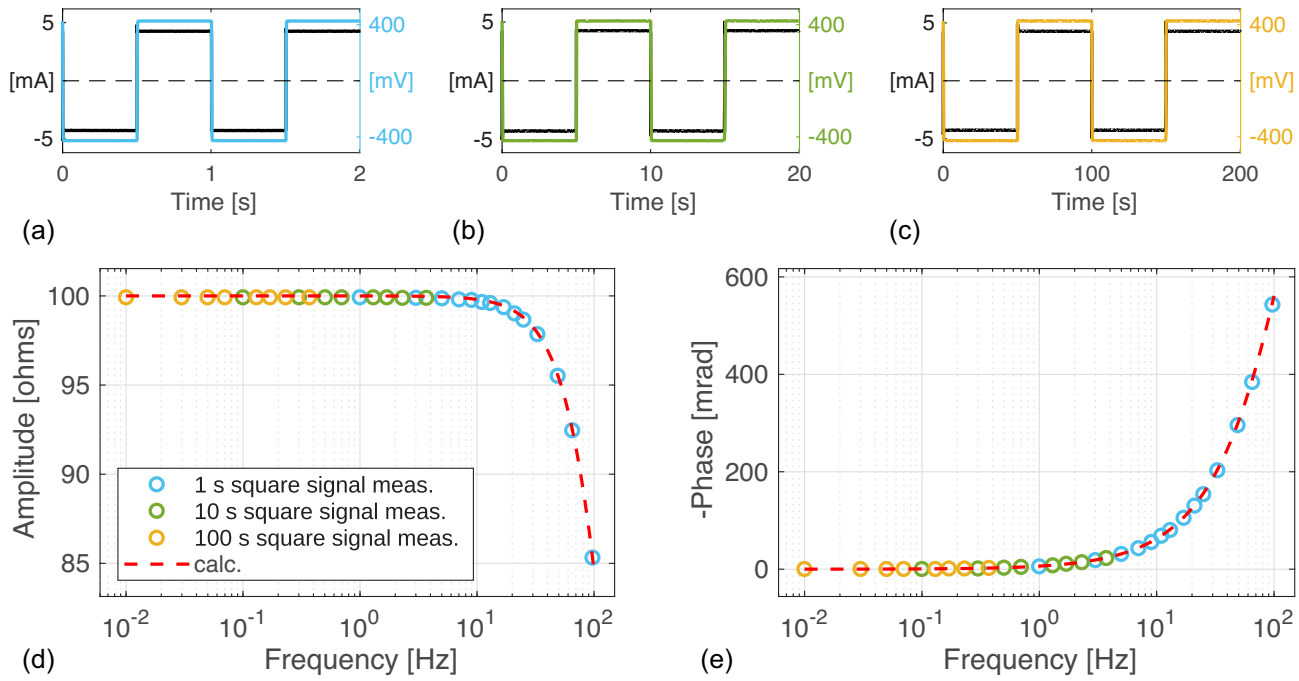

Figure 8. Measurement on an electric circuit with $R = 100\ \Omega$ and $C = 10\ \mu F$ in parallel: (a, b, c) time-domain data of the three signals (1 s-, 10 s- and 100 s-period square-wave signals), in black the injected current, in colour the measured voltage; (d) amplitude and (e) phase of the electrical impedance, described by 14 values from 1 to 97 Hz with the 1 s-period signal, 8 values from 0.1 to 3.7 Hz with the 10 s-period signal, and 8 values from 0.01 to 0.37 Hz with the 100 s-period signal. The theoretical electrical impedance curve is plotted between 0.01 and 100 Hz as a red dotted line.

natural medium is probably due to capacitive effects in the coupling of the electrodes with the medium. The measured electrical impedance values are in very good agreement with the calculated theoretical values (Figs 8d and e): the RMS of the calculated differences at 30 frequencies between 0.01 and 97 Hz is 0.09 Ω and 0.47 mrad.

3.2 *In-situ* comparison with SIP-Fuchs instrument

Next, the performance of the SQWA-SIP system was evaluated *in-situ* by compared with that of the conventional SIP-Fuchs-III instrument. This tool measures spectral impedance point by point by sweeping the frequency band using successive sinusoidal current injections (Radic research—www.radic-research.de). Thus, the acquisition time required to cover the frequency band from 0.01 to 100 Hz is six times longer than with SQWA-SIP instrument: 22 min to inject 16 sinusoidal signals that provide the spectral impedance at 16 logarithmically spaced frequencies, versus 222 s to inject the three square-wave signals that provide the spectral impedance at all their odd harmonics. On-site comparison was made by connecting successively the two instruments to the same electrode device installed in the Guidel wetland. With the SIP-Fuchs, the measurements were made at three depths successively, by connecting the following current and potential dipoles: E7-E8 (electrical impedance at 55 cm depth), E11-E10 (electrical impedance at 70 cm depth) and E15-E14 (electrical impedance at 90 cm depth). As shown in Fig. 9, this yields very consistent IP spectra down to about 0.1 Hz. We often observe that the quality of the data obtained with the 100 s-period square-wave signal is lower than that of the data obtained with the 1 and 10 s-period square-wave signals. This could be explained by the higher noise level recorded at low frequencies, which affects the spectral impedance obtained with the 100 s-period square-wave signal (Fig. 4b) and leads to an increased discrepancy with the SIP-Fuchs data at the lowest frequencies, in amplitude and in phase: the RMS of the differences calculated on the whole data at the three depths, at the harmonics of each of the three square-wave signals, is 0.6 Ω and 4.2 mrad for the 1 s-period signal, 1.5 Ω and 17 mrad for the 10 s-period signal, and 8 Ω and 48 mrad for the 100 s-period signal. In the following section on long-term monitoring in the Guidel wetland ground, we use electrical impedance values at 1 Hz, calculated from the potential spectra with the highest signal-to-noise ratio, as well as maximum phase values above 0.1 Hz where consistency with SIP-Fuchs electrical impedance is good, to analyse the resistivity and phase variations over seven years.

3.3 Long-term monitoring

The SQWA-SIP data recorded in the top metre of soil over more than seven years provide time-lapse 1-D imaging—depth versus time, 6 times a day up to 2021 then twice a day, every 5 cm—of electrical impedance at any selected frequency. Using only data measured with adjacent current and potential dipoles, information is obtained at 14 depths every 5 cm (Fig. 6a). This long-term monitoring data are shown in Fig. 10, for resistivity and phase at 1 Hz, the lowest frequency available since July 2018, and for the maximum phase angle measured since May 2021 at frequencies above 0.1 Hz. Almost every winter, periods of insufficient sunlight to recharge the battery with the solar panel cause the measurements to stop, marked by the white bands across the entire height of the images in Fig. 10 (one month in January 2019, occasionally in January 2021, 10 d in December 2021, 25 d in January 2023, 9 d in November 2023, 11 d in November 2024 and 6 d in January 2025). In addition, a failure of the battery

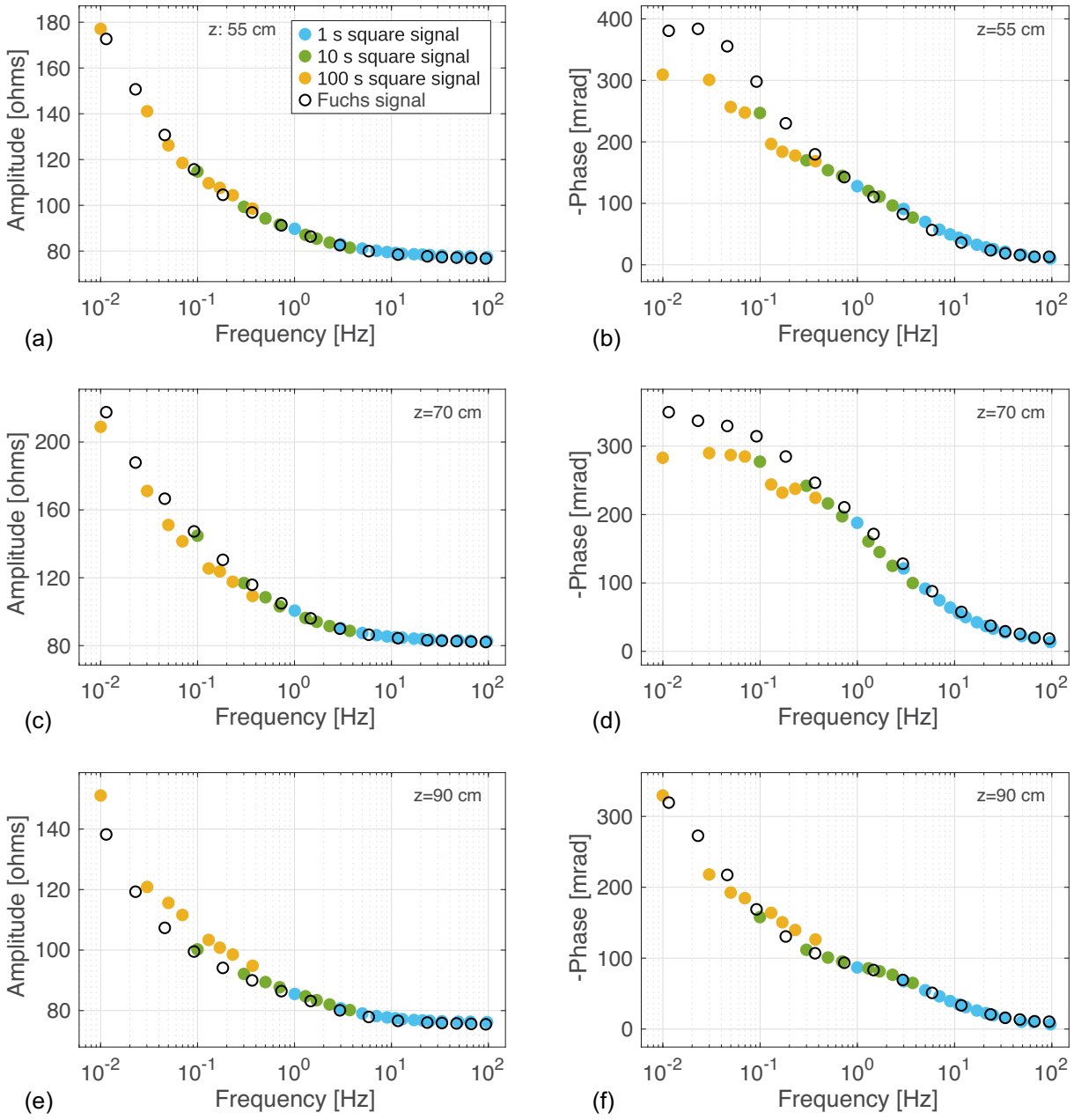

Figure 9. Spectral electrical impedance obtained with the SQWA-SIP system compared to the SIP-Fuchs electrical impedance, measured on the same day at three depths on the field site: (a, c, e) amplitude; (b, d, f) phase angle.

charge controller caused a one-month interruption in measurements during the spring of 2019, and a faulty connection in the data acquisition system led to an interruption in measurements between January and April 2024. Furthermore, a poor connection of the first potential dipole resulted in the absence of measurements at depths of 25 and 30 cm for three periods (nearly three months during the winter of 2020, one month during the winter of 2022 and one month at the end of 2023), and a poor connection of the sixth current dipole resulted in the absence of measurements at depths of 70 and 75 cm for two months during the spring of 2021. With the exception of the data missing due to these device failures, all recorded data are retained for determining electrical impedance.

In Fig. 11, we show that when both are available, phase at 1 Hz and maximum phase vary in the same way. Fig. 12 shows the evolution of resistivity and phase over the seven years at three depths, as well as daily rainfall recorded by a Météo France weather station located 3.5 km away. Large-amplitude spatiotemporal variations are observed for both resistivity and phase, while no clear correlation between the two parameters is observed. The phase time-series are very different at different depths, with the greatest variations observed between 35 and 70 cm depth with no clear trend identified. At some depths, phase varies by up to 150 mrad over time, with a tendency to slow increases and sharp decreases and an absence of clear periodicity. For example, a sharp decrease can be observed at 35 cm

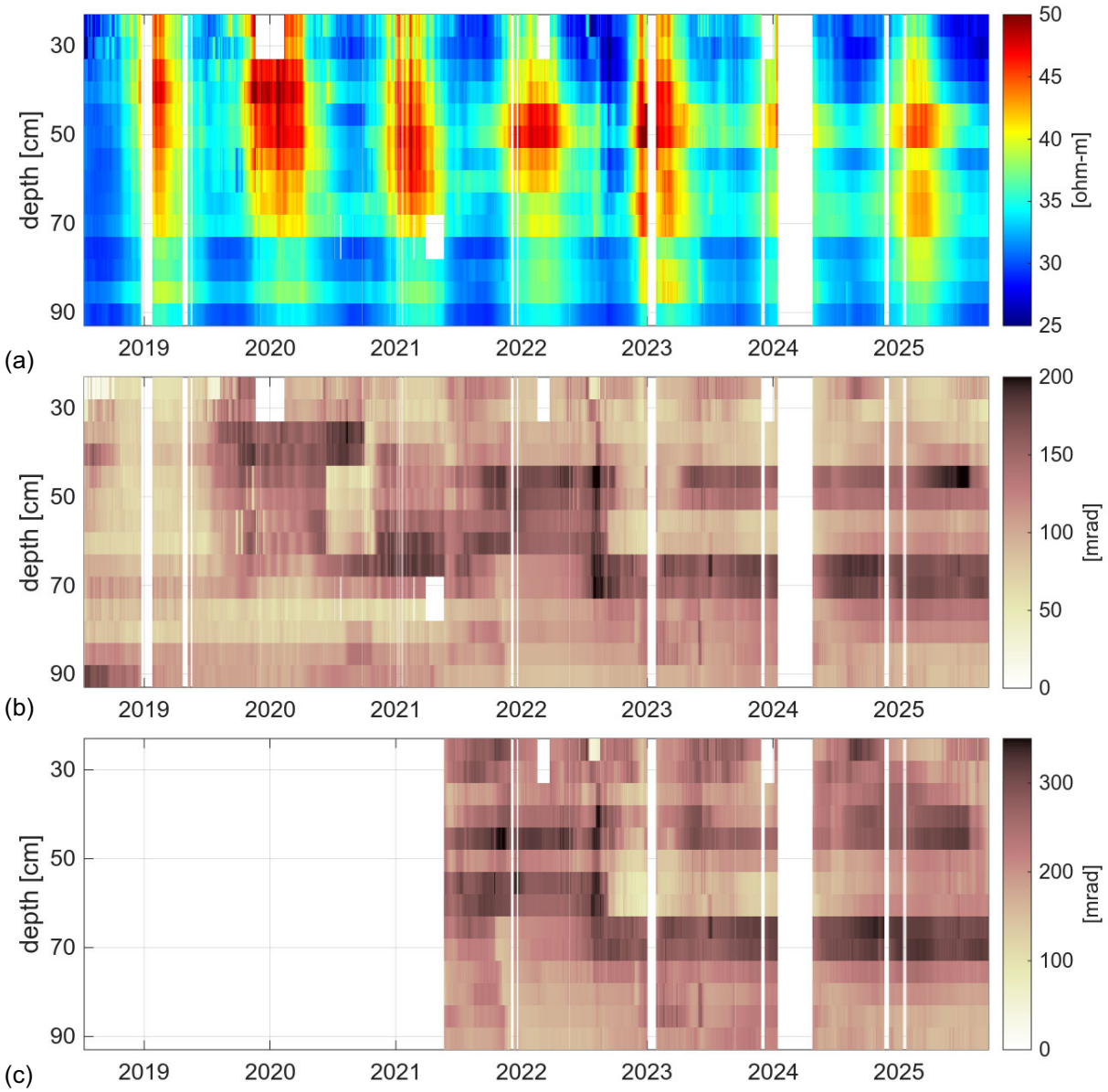

Figure 10. SQWA-SIP data at 14 depths in the Guidel wetland ground: (a) resistivity and (b) phase (opposite sign) measured at 1 Hz since July 2018, (c) maximum phase (opposite sign) measured since May 2021. The white bands across the entire height of the images and the white areas limited to certain depths correspond to missing data due to device failures (poor battery charging or faulty dipole connection).

depth in late 2020, or at 45 cm depth in mid-2020 and late 2022 (Fig. 12). On the other hand, seasonal variations of resistivity are observed, with an amplitude of variations by up to 25 Ω m, yet fading away below 70 cm depth. The highest resistivity values are recorded every winter, while the lowest values are recorded every summer (Figs 10a and 12).

The influence of seasonal temperature variations on resistivity could be analysed using data recorded between July 2018 and December 2020, a period when PT100 sensors continuously recorded the temperature in the ground next to the electrode rods, at five depths between 15 and 125 cm. Figs 13(a) and (c) show the correlation between measured conductivity at 1 Hz and temperature at two different depths, with an average linear fit coefficient equal to 0.85 mS m^{-1}°C^{-1}. In contrast, no clear correlation is observed between electrical impedance phase at 1 Hz and temperature (Figs 13b and d). Subtracting the influence of temperature provides corrected resistivity time-series that still vary with similar amplitude but with a less marked periodicity. The actual persistence of a periodicity after correction even remains uncertain, due to the limited period of soil temperature recording.

4. DISCUSSION

4.1. Discrepancy between SQWA-SIP and SIP-Fuchs data at low frequency

We observe on Fig. 9 a very good agreement between SQWA-SIP and SIP-Fuchs impedance spectra, which worsens when electrical impedance is measured with the injection of 100 s square-wave signal, that is, for frequencies below 0.1 Hz. Although the cause of this discrepancy has not yet been identified clearly, it

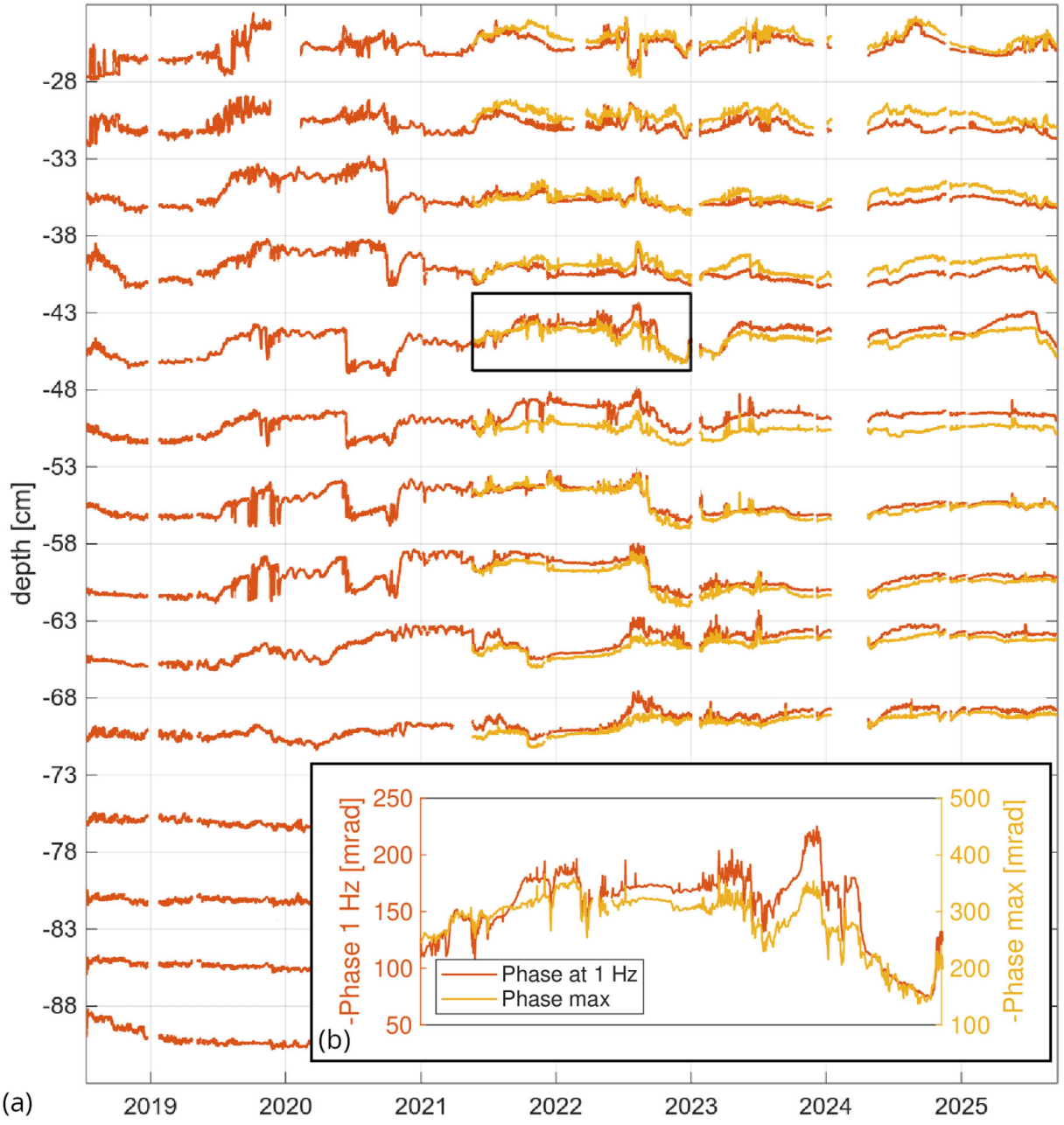

Figure 11. Electrical impedance phase at 1 Hz since July 2018 (brown lines) and maximum value since May 2021 (yellow lines): (a) at 14 depths during the whole period; (b) at 45 cm depth between May 2021 and December 2022.

could be explained by the presence of a $1/f$ noise, which more significantly affects the spectral impedance obtained with the 100 s-period square-wave signal. In order to rule out possible effects from the SQWA-SIP internal circuits, the SQWA-SIP system was validated in the laboratory on a calibrated RC circuit, without the electrode rods. In the future, other experiments using both the SQWA-SIP and the SIP-Fuchs instruments will be carried out at different test sites.

4.2. Perspective for SQWA-SIP development

Currently, the electrode device consists of two parallel rods a few tens of centimetres apart with electrodes every 5 cm, and the injected current is limited to ± 4 mA. Moreover, the electrodes are hard-wired between the rods to form eight current dipoles alternating with seven potential dipoles (Fig. 6a). When a current injection is performed from a dipole, the eight-channel measuring device records the injected current and the seven voltage signals. In practice, however, only the voltage measured at the adjacent electrodes of the current injection dipole is used, as the voltage detected at the more distant electrodes is not sufficient for SIP analysis. Since the maximum injected current is determined by the power source and its autonomy, increasing the injected current would mean adding a renewable source of power, such as wind-turbine. This would allow increasing the voltage level further away from the current electrodes. Nevertheless, with

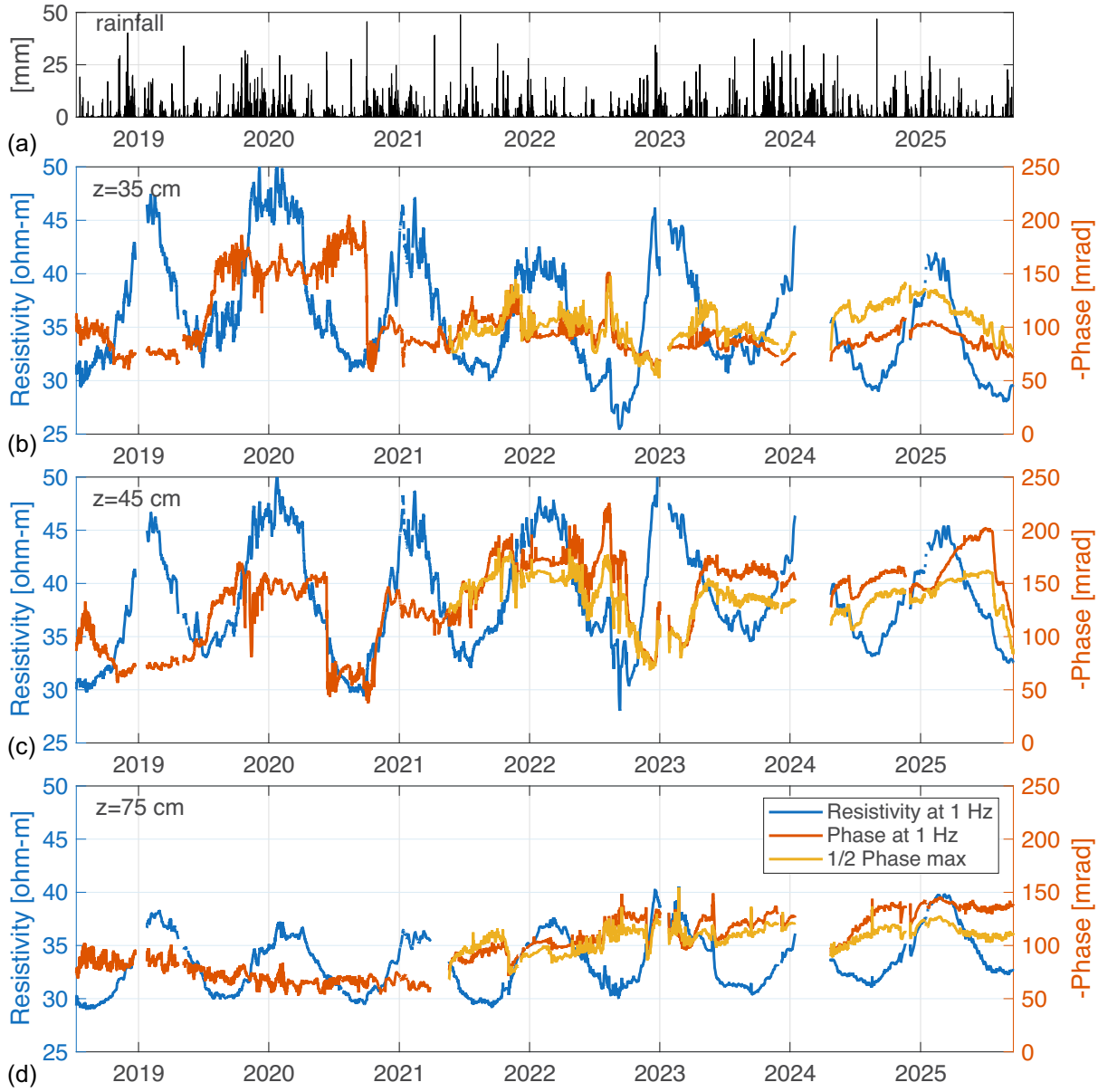

Figure 12. SQWA-SIP data at the Guidel wetland: (a) rainfall recorded at a Météo France weather station 3.5 km away; (b, c, d) electrical impedance (complex resistivity) at three depths since July 2018.

the equatorial electrode configuration in which the system is currently locked, this would not add much information, as it would not allow meaningful 2-D inversion. On the other hand, integrating a relay switch to the system would allow diversification of the electrode configurations and thus exploiting all the channels as well as providing a meaningful data set for 2-D inversion. In such a context, reinforcing the power source may also be beneficial. The intention is to reproduce the instrument and improve it each time, taking into account new developments that remain at a reasonable cost.

The decrease in data quality below 0.1 Hz, and the corresponding discrepancy with the SIP-Fuchs instrument, limit the spectral analysis at this stage. Fixing this issue would allow further exploitation of the spectral content of the signal, with, for example, Debye decomposition of the spectrum or Cole–Cole inversion.

4.3. Origin of large phase angle variations

While a certain periodicity is observed for the resistivity signal (in blue on Fig. 12) which can be at least attributed partly to subsurface temperature variations (Figs 13a and c), the electrical impedance phase (in brown/yellow on Fig. 12) does not follow the same periodicity and does not seem significantly influenced by temperature variations (Figs 13b and d).

Overall, the phase angle variations (including both the maximum phase angle, in yellow, and the phase angle at 1 Hz, in brown) are irregular over the monitoring period. A certain

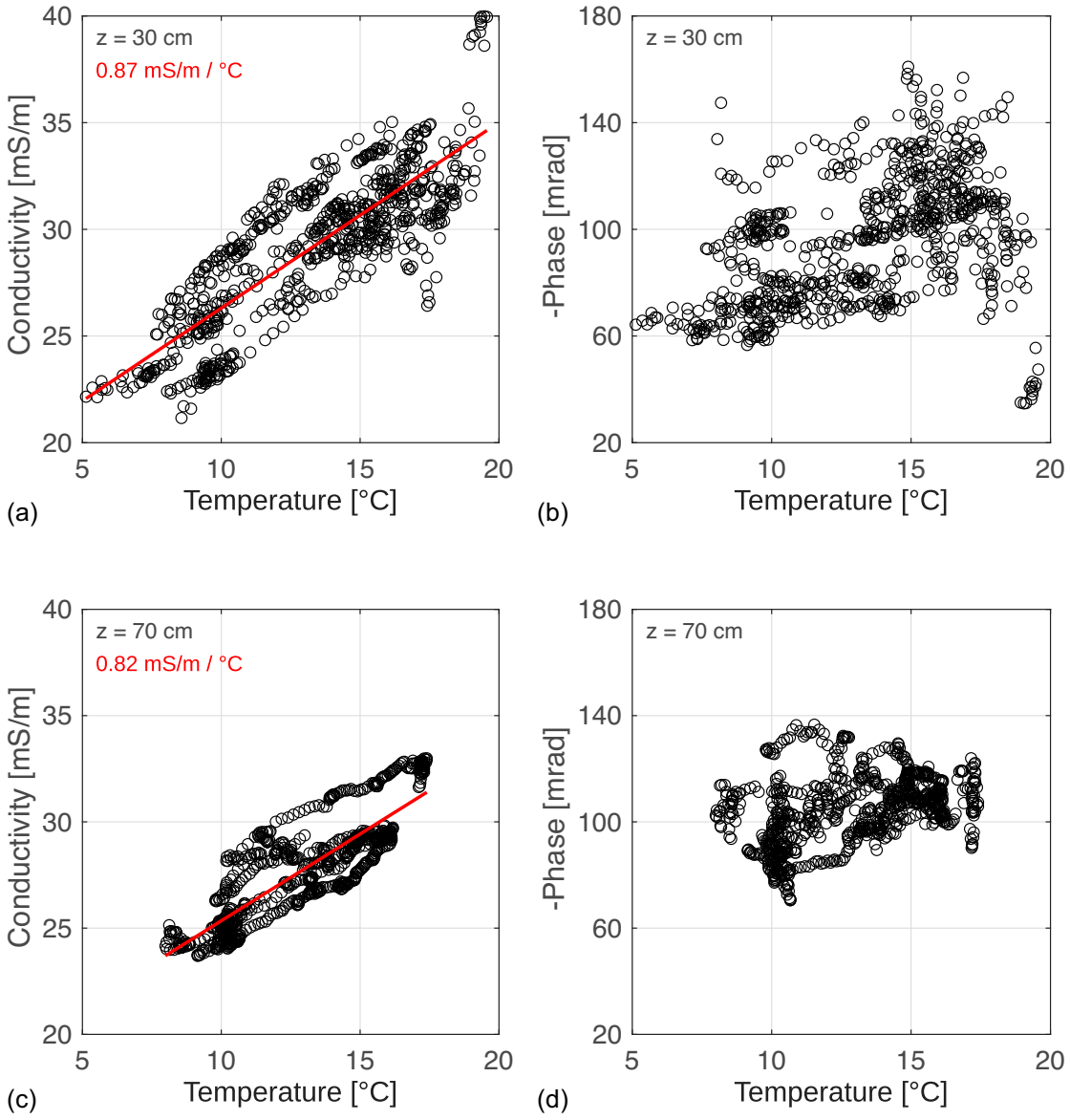

Figure 13. Data recorded in the wetland ground between July 2018 and December 2020: (a, c) SQWA-SIP conductivity at 1 Hz versus temperature at depths of 30 and 70 cm (black circles) and linear fit (red line); (b, d) SQWA-SIP phase at 1 Hz versus temperature at the same depths.

consistency is observed over depth (Fig. 10) although (i) similar changes may happen at different times in different depth ranges and (ii) changes observed in a certain depth ranges do not happen outside this range. For example, a sharp drop from 200 to 50 mrad is observed in late 2020 at 35 cm depth, while a similar drop—from 150 to 50 mrad—is observed earlier at 45 cm depth (Fig. 12). This drop happens at the same time at depths 35 and 40 cm, and at an earlier time at depths 45–60 cm, while it does not happen at depth shallower than 35 cm or deeper than 60 cm (Fig. 10 and 11). Furthermore, the phase angle at 45 cm increases back to its high level at the beginning of 2021, while such an increase is not observed at 35 cm (Fig. 12). This illustrates the relevance of monitoring the phase signal with high spatial and temporal resolution to understand critical zone processes.

Given the large amplitude of the phase angle variations over the monitoring period (150 mrad), as well as the variable rates of increase and decrease, up to 50 mrad d^{-1}, we suggest that cycles of dissolution–precipitation–passivation of metallic sulfides may be responsible to a large extent for the signal. Column experiments involving precipitation–passivation of iron sulfide minerals observe variations up to 60 mrad with both increases and decreases of the signal (K.H. Williams *et al.* 2005; L. Slater *et al.* 2007). Laboratory experiments on volcanic samples from hydrothermal areas containing naturally occurring iron sulfide minerals measure phase angle in the range 0–200 mrad, with the highest values being attributed to pyrrhotite rather than pyrite (L. Lévy *et al.* 2019). Conditions are met at Guidel wetland for sulfate reduction—high concentrations of organic matter and sulfate, generally anoxic conditions, presence of sulfate-reducing bacteria in metagenomic analysis (unpublished data)—and subsequence metallic sulfide precipitation with high concentration of iron in circulation (I. Osorio-Leon *et al.* 2023). In this low-temperature, dynamic context, iron-sulfides with

a formula closer to FeS (such as mackinawaite) than to FeS2 (pyrite) are expected. In addition, periodic oxygen arrival should be able to trigger abrupt dissolution, or passivation, of iron sulfide minerals. Other critical zone processes may also be responsible for the observed phase angle variations: temporary chemical disequilibrium related to precipitation and dissolution of other minerals (S. Izumoto *et al*. 2022; F. Rembert *et al* 2024) or microbial activity (A. Mellage *et al*. 2018). Nevertheless, laboratory experiments studying the influence of biofilm and microbial growth on the phase angle show that (i) biofilm growth does not clearly influence the phase angle—although it can significantly decrease the resistivity (P. Kessouri *et al*. 2019; C.L. Rosier *et al*. 2019) and (ii) the phase angle increase attributed to microbial growth in these experiments is less than 3 mrad (A. Mellage *et al*. 2018; C.L. Rosier *et al*. 2019). Further work is needed to interpret the origin of the phase variations, including *in-situ* experiments, geochemical monitoring and reactive transport modelling.

5. CONCLUSION

A new SIP instrument called SQWA-SIP has been developed and installed at a field site for monitoring natural wetland processes for more than seven years. The instrument is plugged onto two 1-m-long vertical rods with 15 electrodes each, offering 1-D vertical imaging in the top metre of soil with high spatial resolution, in the order of 5 cm. Thanks to the injection of three square-wave signals with different periods and to the high sampling rate for recording both the voltage and current signals, a Fourier transform-based algorithm was implemented to recover spectral information from the square-wave signal. On-site comparison with a conventional SIP-Fuchs instrument plugged to the same electrodes yields very consistent IP spectra down to 0.1 Hz. Data quality decreases below 0.1 Hz, which corresponds to an increased discrepancy with the SIP-Fuchs for certain dates and electrode configurations. Compared to a SIP-Fuchs instrument, the acquisition time is divided by 6 to recover the same spectral information between 0.01 and 100 Hz. Spectral analysis of the recorded signals provides time-lapse 1-D imaging—depth versus time, twice a day, every 5 cm—of the maximum phase angle, $\phi_{\max}$, and the DC resistivity, ρ_{DC}, in the top metre of soil.

Large-amplitude spatiotemporal variations are observed for both ρ_{DC} and $\phi_{\max}$, while no clear correlation between the two parameters is observed. At certain depths, $\phi_{\max}$ varies by up to 150 mrad over time, with a tendency to slow increases and sharp decreases and an absence of clear periodicity. Moreover, the $\phi_{\max}$ time-series differ in different depth ranges. On the other hand, seasonal variations of ρ_{DC} are observed, with an amplitude of variations by up to 25 Ωm, yet fading away below 60 cm depth. The influence of seasonal temperature variations on ρ_{DC} was confirmed by temperature sensors continuously recording the soil temperature during a 29-month period where temperature sensors continuously recorded the temperature in the soil. Possible causes of $\phi_{\max}$ variations over time include metallic sulfide precipitation through sulfate reduction in this generally anoxic environment, combined with irregular discharge of highly oxic waters into the wetland that may trigger precipitation and passivation processes. Other processes such as temporary chemical disequilibrium and microbial activity may be responsible for part of the observed variations.

ACKNOWLEDGMENTS

The authors would like to thank the anonymous reviewers for their very constructive suggestions and comments. This work received financial support from the state managed by the National Agency for Research under the Future Investment Program integrated into France 2030, with reference ANR-21-ESRE-0014 (https://terra-forma-web.osug.fr/), as well as Blue Transition INTERREG project (https://www.interregnorthsea.eu/blue-transition). Guidel observatory is part of the network of hydrogeological observatories (SNO H+, https://hplus.ore.fr/en/ploemeur/) and OZCAR research infrastructure (https://www.ozcar-ri.org/).

DATA AVAILABILITY

One raw data set and the Matlab code for calculating complex conductivity spectra are available in the SNO H + data base and can be downloaded from the following address: https://doi.org/10.26169/hplus.guidel_spectral_induced_polarization.

REFERENCES

Bertin, J. & Loeb, J., 1976. *Experimental and Theoretical Aspects of Induced Polarization*. Vol., **1,** 250pp, Schweizerbart Science Publishers.

Binley, A. & Slater, L., 2020. *Resistivity and Induced Polarization: Theory and Applications to the Near-Surface Earth*. Cambridge Univ. Press.

Blanchy, G., Deroo, W., De Swaef, T., Lootens, P., Quataert, P., Roldán-Ruíz, I., Versteeg, R. & Garré, S., 2025. Closing the phenotyping gap with non-invasive belowground field phenotyping, *soil.,* **11**(1), 67–84.

Carrière, S.D., *et al.* 2021. First evidence of correlation between evapotranspiration and gravity at a daily time scale from two vertically spaced superconducting gravimeters, *Geophys. Res. Lett.,* **48**(24), e2021GL096579. doi: 10.1029/2021GL096579.

Dahlin, T. & Leroux, V., 2012. Improvement in time-domain induced polarization data quality with multi-electrode systems by separating current and potential cables, *Near Surf. Geophys.,* **10**(6), 545–565.

Dumont, M. & Singha, K., 2024. Geophysics as a hypothesis-testing tool for critical zone hydrogeology, *Wiley Interdisciplinary Rev.: Water,* **11,** e1732. doi: 10.1002/wat2.1732.

Fiandaca, G., Ramm, J., Binley, A., Gazoty, A., Christiansen, A.V. & Auken, E., 2013. Resolving spectral information from time domain induced polarization data through 2-d inversion, *Geophys. J. Int.,* **192,** 631–646.

Flores Orozco, A., Williams, K.H., Long, P.E., Hubbard, S.S. & Kemna, A., 2011. Using complex resistivity imaging to infer biogeochemical processes associated with bioremediation of an uranium-contaminated aquifer, *J. geophys. Res.: Biogeosciences,* **116**(G3). doi: 10.1029/2010JG001591.

Gaillardet, J., 2023. *La Terre habitable ou l'épopée de la zone critique.* La Découverte.

Gaillardet, J., *et al.* 2018. OZCAR: the French network of critical zone observatories, *Vadose Zone J.,* **17**(1), 1–24.

Guillaumot, L., Longuevergne, L., Marçais, J., Lavenant, N. & Bour, O., 2022. Frequency domain water table fluctuations reveal impacts of intense rainfall and vadose zone thickness on groundwater recharge, *Hydrol. Earth Syst. Sci.,* **26**(22), 5697–5720.

Gurin, G., Tarasov, A., Ilyin, Y. & Titov, K., 2013. Time domain spectral induced polarization of disseminated electronic conductors: laboratory data analysis through the Debye decomposition approach, *J. Appl. Geophys.,* **98,** 44–53.

Hermans, T., *et al.* 2023. Advancing measurements and representations of subsurface heterogeneity and dynamic processes: towards 4D hydrogeology, *Hydrol. Earth Syst. Sci.,* **27**(1), 255–287.

Hu, K., Jougnot, D., Huang, Q., Looms, M.C. & Linde, N., 2020. Advancing quantitative understanding of self-potential signatures in the

critical zone through long-term monitoring, *J. Hydrol.,* **585,** 124771. doi: 10.1016/j.jhydrol.2020.124771.

Izumoto, S., *et al.* 2022. Pore-scale mechanisms for spectral induced polarization of calcite precipitation inferred from geo-electrical millifluidics, *Environ. Sci. Technol.,* **56**(8), 4998–5008.

Jayawickreme, D.H., Van Dam, R.L. & Hyndman, D.W., 2010. Hydrological consequences of land-cover change: quantifying the influence of plants on soil moisture with time-lapse electrical resistivity, *Geophysics,* **75,** WA43–WA50.

Johansson, S., Hedblom, P. & Dahlin, T., 2020. Spectral analysis of time domain induced polarization waveform, *J. Appl. Geophys.,* **177,** 104037. doi: 10.1016/j.jappgeo.2020.104037.

Kessouri, P., *et al.* 2019. Induced polarization applied to biogeophysics: recent advances and future prospects, *Near Surf. Geophys.,* **17**(6-Recent Developments in Induced Polarization), 595–621.

Lévy, L., Ciraula, D.A., Legros, B., Martin, T. & Weller, A., 2024. Understanding the fate of H2S injected in basalts by means of time-domain induced polarization geophysical logging, *J. geophys. Res.: Solid Earth,* **129**(6), e2023JB028316.

Lévy, L., Gibert, B., Sigmundsson, F., Parat, F., Deldicque, D. & Hersir, G.P., 2019. Tracking magmatic hydrogen sulphur circulations using electrical impedance: complex electrical properties of core samples at the Krafla volcano, Iceland, *J. geophys. Res.: Solid Earth,* **124**(3), 2492–2509.

Liu, W., Chen, R., Cai, H., Luo, W. & Revil, A., 2017. Correlation analysis for spread-spectrum induced polarization signal processing in electromagnetically noisy environments, *Geophysics,* **82**(5), E243–E256.

Liu, W., Lü, Q., Chen, R., Lin, P., Chen, C., Yang, L. & Cai, H., 2019. A modified empirical mode decomposition method for multiperiod time-series detrending and the application in full-waveform induced polarization data, *Geophys. J. Int.,* **217**(2), 1058–1079.

Martin, T., Titov, K., Tarasov, A. & Weller, A., 2021. Spectral induced polarization: frequency domain versus time domain laboratory data, *Geophys. J. Int.,* **225**(3), 1982–2000.

Mary, B., Peruzzo, L., Boaga, J., Cenni, N., Schmutz, M., Wu, Y., Hubbard, S.S. & Cassiani, G., 2020. Time-lapse monitoring of root water uptake using electrical resistivity tomography and mise-à-la-masse: a vineyard infiltration experiment, *Soil.,* **6,** 95–114.

Mellage, A., Smeaton, C.M., Furman, A., Atekwana, E.A., Rezanezhad, F. & Van Cappellen, P., 2018. Linking spectral induced polarization (SIP) and subsurface microbial processes: results from sand column incubation experiments, *Environ. Sci. Technol.,* **52**(4), 2081–2090.

Nordsiek, S. & Weller, A., 2008. A new approach to fitting induced-polarization spectra, *Geophysics,* **73**(6), F235–F245.

Norooz, R., Nivorlis, A., Olsson, P.I., Günther, T., Bernstone, C. & Dahlin, T., 2024. Monitoring of Älvkarleby test embankment dam using 3D electrical resistivity tomography for detection of internal defects, *J. Civil Struct. Health Monit.,* **14**(5), 1275–1294.

Ntarlagiannis, D., Williams, K.H., Slater, L. & Hubbard, S., 2005. Low-frequency electrical response to microbial induced sulfide precipitation, *J. geophys. Res.: Biogeosciences,* **110**. doi: 10.1029/2005JG000024.

Osorio-Leon, I., Bouchez, C., Chatton, E., Lavenant, N., Longuevergne, L. & Le Borgne, T., 2023. Hydrological and Geological Controls for the Depth Distribution of Dissolved Oxygen and Iron in Silicate Catchments, *Water Resour. Res.,* **59,** e2023WR034986. doi: 10.1029/2023WR034986.

Rembert, F., Leroy, P., Lassin, A. & Roman, S., 2024. Microfluidics and spectral induced polarization for direct observation and petrophysical modeling of calcite dissolution, *Geophys. Res. Lett.,* **51**(24), e2024GL111271. doi: 10.1029/2024GL111271.

Rosier, C.L., Atekwana, E.A., Aal, G.A. & Patrauchan, M.A., 2019. Cell concentrations and metabolites enhance the SIP response to biofilm matrix components, *J. Appl. Geophys.,* **160,** 183–194.

Schlumberger, C., 1920. *Etude sur la prospection électrique du sous-sol*. Gauthier-Villars.

Slater, L., Ntarlagiannis, D., Personna, Y.R. & Hubbard, S., 2007. Pore-scale spectral induced polarization signatures associated with FeS biomineral transformations, *Geophys. Res. Lett.,* **34**. doi: 10.1029/2007GL031840.

Slater, L.D., Ntarlagiannis, D., Day-Lewis, F.D., Mwakanyamale, K., Versteeg, R.J., Ward, A. & Lane, J.W., Jr., 2010. Use of electrical imaging and distributed temperature sensing methods to characterize surface water–groundwater exchange regulating uranium transport at the Hanford 300 Area, Washington, *Water Resour. Res.,* **46**. doi: 10.1029/2010WR009110.

Steelman, C.M., Klazinga, D.R., Cahill, A.G., Endres, A.L. & Parker, B.L., 2017. Monitoring the evolution and migration of a methane gas plume in an unconfined sandy aquifer using time-lapse GPR and ERT, *J. Contam. Hydrol.,* **205,** 12–24.

Sumner, J.S., 1976. *Principles of Induced Polarization for Geophysical Exploration.* Elsevier Scientific Publishing.

Titov, K., Kemna, A., Tarasov, A. & Vereecken, H., 2004. Induced polarization of unsaturated sands determined through time domain measurements, *Vadose Zone J.,* **3**(4), 1160–1168.

Titov, K., Komarov, V., Tarasov, V. & Levitski, A., 2002. Theoretical and experimental study of time domain-induced polarization in water-saturated sands, *J. Appl. Geophys.,* **50**(4), 417–433.

Tong, M. & Tao, H., 2007. Experimental study of induced polarization relaxation time spectra of shaly sands, *J. Pet. Sci. Eng.,* **59**(3-4), 239–249.

Voytek, E.B., Barnard, H.R., Jougnot, D. & Singha, K., 2019. Transpiration-and precipitation-induced subsurface water flow observed using the self-potential method, *Hydrol. Processes,* **33**(13), 1784–1801.

Williams, K.H., *et al.* 2009. Geophysical monitoring of coupled microbial and geochemical processes during stimulated subsurface bioremediation, *Environ. Sci. Technol.,* **43**(17), 6717–6723.

Williams, K.H., Ntarlagiannis, D., Slater, L.D., Dohnalkova, A., Hubbard, S.S. & Banfield, J.F., 2005. Geophysical Imaging of Stimulated Microbial Biomineralization, *Environ. Sci. Technol.,* **39,** 7592–7600.